Apparent Absorption of Solar Spectral Irradiance in Heterogeneous Ice Clouds

K. Sebastian Schmidt[1][*], Peter Pilewskie[1], Bernhard Mayer[2,3], Manfred Wendisch[4],

Bruce Kindel[1], Steven Platnick[5], Michael D. King[1], Gala Wind[5,6], G. Tom Arnold[5,6],

Lin Tian[5], Gerald Heymsfield[5], Heike Eichler[7]

[1] University of Colorado, Boulder, CO, USA

[2] Deutsches Zentrum für Luft- und Raumfahrt (DLR), Oberpfaffenhofen, Germany

[3] Ludwig-Maximilians-Universität, Munich, Germany

[4] Leipzig Institute for Meteorology, Universität Leipzig, Germany

[5] Goddard Space Flight Center, Greenbelt, MD, USA

[6] SSAI, Inc., Lanham, MD, USA

[7] Institute for Atmospheric Physics, Universität Mainz, Germany

[*] Corresponding author: K. Sebastian Schmidt, Laboratory for Atmospheric and Space Physics, University of Colorado, 392 Campus Box, Boulder, Colorado, USA. Phone: 303-492-6401. Email Sebastian.Schmidt@lasp.colorado.edu

1

21   Abstract:

22   Coordinated flight legs of two aircraft above and below extended cirrus cloud scenes

23   played an important part in the Tropical Composition, Cloud and Climate Coupling (TC[4])

24   Experiment (Costa Rica, 2007). The Solar Spectral Flux Radiometer (SSFR) measured

25   up- and downward irradiance on the high-altitude (ER-2) and the low-altitude (DC-8)

26   aircraft, which allowed deriving apparent absorption on a point-by-point basis along the

27   flight track. Apparent absorption is the vertical divergence of irradiance, calculated by the

28   difference of net flux at the top and bottom of a cloud. While this is the only practical

29   method of deriving absorption from aircraft radiation measurements, it differs from true

30   absorption when horizontal flux divergence is non-zero. Differences between true and

31   apparent absorption are inevitable in any inhomogeneous atmospheres, especially clouds.

32   We show, for the first time, the spectral shape of measured apparent absorption and

33   compare with results from a three-dimensional radiative transfer model. The model cloud

34   field is created from optical thickness and effective radius retrievals from the MODIS

35   (Moderate Resolution Imaging Spectroradiometer) Airborne Simulator (MAS), and from

36   reflectivity profiles from the Cloud Radar System (CRS), both onboard the ER-2.

37   Although the spectral shape is reproduced by the model calculations, the measured

38   apparent absorption in the visible spectral range is higher than the model results along

39   extended parts of the flight leg. This is possibly due to a net loss of photons into

40   neighboring cirrus-free areas that are not contained within the boundaries of the model

41   domain.

42

1. Introduction

The issue of real versus apparent absorption of solar radiation within clouds was discussed for decades after *Fritz and MacDonald* [1951] discovered cloud absorption derived from measurements may far exceed that from model calculations. Despite its significance for atmospheric energy budget assessments, cloud dynamics, and remote-sensing, a conclusive explanation for this persistent bias is still lacking, and it re-emerges regularly in literature. At best, a status quo was achieved where some authors argued that the problem is ill-posed because the measurement (or model) errors are too large for a final assessment of the bias, while others found model-measurement agreement within the given uncertainties. *Stephens and Tsay* [1990] reviewed the observational evidence for various manifestations of the effect and summarized explanations for the discrepancies. Thereafter, a controversial discussion was initiated by new observations [*Cess et al.*, 1995; *Ramanathan et al.*, 1995; *Pilewskie and Valero*, 1995]. Based on a range of conditions, follow-up studies either rejected [*Hayasaka et al.*, 1995; *Arking*, 1996; *Stephens*, 1996; *Taylor et al.*, 1996; *Francis et al.*, 1997; *Ackerman et al.*, 2003] or supported [*Pilewskie and Valero* 1996, *Valero et al.*, 1997; *Zhang et al.*, 1997; *Valero et al.*, 2000; *O'Hirok et al.*, 2000; *O'Hirok and Gautier*, 2003] the existence of a bias. Many studies favored horizontal photon transport in heterogeneous clouds as cause for the discrepancies [*Newiger and Baehnke*, 1981; *Ackerman and Cox*, 1981; *Rawlins*, 1989; *Titov*, 1998; *Marshak et al.*, 1997, 1998 and 1999; Harshvardhan et al., 1998] although other explanations were suggested such as enhanced in-cloud water vapor absorption [e.g., *Francis et al.*, 1997; *Arking*, 1999], large drop contributions [*Wiscombe et al.*,

66 1984; *Ackerman and Stevens*, 1987; *Knyazikhin et al.*, 2002], or in-cloud aerosols

67 [*Newiger and Baehnke*, 1981; *Chylek et al.*, 1984 and 1996, *Wendisch and Keil*, 1999].

68

69 Certainly, discrepancies may be caused by a combination of multiple effects, all of which

70 can be ascribed to inappropriate model assumptions or insufficient observations. When

71 attributing shortwave absorption biases to individual causes, adequate spectral resolution

72 in models and measurements to separate the roles of gas and condensed species is highly

73 valuable. For example, absorption by water vapor, aerosol, liquid water or ice can be

74 distinguished by spectral signatures, whether or not the absorption is enhanced due to

75 photon path lengthening in heterogeneous clouds. Most experiments, especially before

76 the late 1990s, did not make use of spectrally resolved measurements. Instruments with

77 full spectral coverage over the solar wavelength range were introduced by *Pilewskie et al.*

78 [2003] and *Wendisch et al.* [2001] for use in aircraft experiments. Despite this important

79 advancement in measurement technology, aspects of the absorption bias problem

80 lingered, for a number of reasons: In typical experiments, absorbed irradiance is derived

81 by differencing net irradiance (difference of downward and upward irradiance) at cloud

82 base and cloud top. This introduces large systematic errors in estimates of cloud

83 absorption because it is the (small) difference of four large quantities. If the

84 measurements above and below clouds are not coordinated in time and space, cloud

85 heterogeneities add further uncertainty. Even if they are coordinated, the measurements

86 may be affected by a net transport of photons through the sides of the sampling volume

87 (net horizontal photon outflux or influx). Horizontal irradiance divergence (convergence)

88 is balanced by the vertical flux divergence which can be misinterpreted as true

89   absorption. We refer to vertical flux divergence as apparent absorption, different from

90   true absorption by the magnitude of horizontal flux divergence.

91

92   Horizontal photon transport can be understood in the context of radiative smoothing.

93   Over some scale, contrasts in cloud optical thickness are smoothed out in the

94   corresponding reflectance and transmittance fields [*Marshak et al.*, 1995]. For cloud

95   fields with shadow effects (i.e. clouds with pronounced vertical structure) a roughening

96   can occur as well [*Marshak et al.*, 2006]. For the case of smoothing, the horizontal

97   displacement of a photon relative to its entrance into a cloud field is determined by the

98   number of scatterings it undergoes, and by the asymmetry parameter. The photon

99   transport is always directed from higher to lower photon density. *Platnick* [2001] shows

100   that this characteristic distance is a function of wavelength (that is, single scattering

101   albedo and asymmetry parameter). In absence of shadows and sources, the horizontal re-

102   distribution of photons in a smoothing process as seen from space (reflectance) can be

103   viewed as transport from optically thick to optically thin regions within the characteristic

104   smoothing scale. The photon path length distribution associated with these processes can

105   be fundamentally different for optically thick regions (diffusion regime) and thin,

106   sparsely populated areas [*Davis and Marshak*, 2000].

107

108   Various methods were proposed to correct for horizontal flux divergence in aircraft

109   measurements of absorption. *Ackerman and Cox* [1981] introduced a technique for

110   sampling radiation with a combination of broadband and filter radiometers. Absorption

111   measurements were corrected under the assumption that clouds do not absorb in the

112   visible wavelength range and that radiative smoothing affects non-absorbing and

113   absorbing wavelengths equally. *Marshak et al.* [1999] suggested various correction

114   schemes. One of these explicitly takes into account a pre-determined radiative smoothing

115   scale. Although this improves the Ackerman and Cox method considerably, it does not

116   entirely reproduce the true absorption. *Titov* [1998] (among others) suggested averaging

117   of cloud absorption measurements over the entire flight leg and provided minimum

118   domain sizes based on typical boundary layer clouds.

119

120   In this paper, we pursue a different strategy. Since true absorption is difficult to derive

121   from measurements, we focus on apparent absorption, as obtained from two-aircraft

122   observations, and we reproduce measured apparent spectral absorption (vertical flux

123   divergence) on a pixel-by-pixel basis with 3D radiative transfer (RT) calculations. This

124   strategy is akin to that used by *O'Hirok and Gautier* [2003] who employed ground-based

125   cloud observations as input to 3D RT calculations. We used airborne measurements from

126   the NASA TC^4 experiment (Tropical Composition Cloud and Climate Coupling, Costa

127   Rica, 2007: *Toon et al.*, 2009). An extensive set of instruments was deployed onboard

128   two aircraft, the NASA ER-2 and DC-8. The Solar Spectral Flux Radiometer (SSFR:

129   *Pilewskie et al.*, 2003) was flown on both platforms and measured spectrally-resolved

130   upward and downward solar irradiance. The ER-2 carried the MODIS (Moderate

131   Resolution Imaging Spectroradiometer) airborne simulator (MAS: *King et al.*, 1996), the

132   cloud radar system (CRS: *Li et al.*, 2004), and other remote-sensing instruments. It was

133   operated at 20 km altitude – well above cloud top level. The DC-8 was flown within and

134   below cloud layers and was equipped with instrumentation for cloud microphysical,

135 aerosol particle, and gas-phase measurements. On seven flight days, the ER-2 and DC-8

136 were closely coordinated (in space and time) along several flight legs (typically about a

137 1/2 hour duration per leg) that were chosen in outflow regions near tropical cloud

138 convective cells. In this way, detailed cloud structure data were acquired along with

139 simultaneous above- and below-cloud measurements of solar spectral irradiance.

140 Measurements of cloud-reflected radiance were used for the retrieval of cloud optical

141 thickness and particle size.

142

143 We determined point-by-point apparent spectral absorption for one case and compared

144 with model results. The calculated irradiance fields were obtained from 3D RT

145 calculations, using measurements from MAS and CRS to derive the input cloud field.

146

147 The paper starts with a brief description of the instruments, measurement strategy, data

148 processing, generation of the 3D cloud, and of the 3D RT model (section 2). Results are

149 presented in section 3. In the conclusions (section 4), possible implications for remote-

150 sensing and atmospheric energy budget are discussed.

151

152 2. Instruments, data, and radiative transfer calculations

153

154 Solar Spectral Flux Radiometer

155 The SSFR [*Pilewskie et al.*, 2003] measured spectral shortwave irradiance on the ER-2

156 (above clouds), and on the DC-8 below or within clouds. On both platforms, the up- and

157 down-looking optical inlets were fix-mounted on the aircraft fuselage and connected to

158   rack-mounted spectrometers though optical fibers. The spectral range (350-2150 nm) was

159   covered by using two spectrometers per optical inlet: a grating spectrometer with a

160   Silicon CCD array for near-ultraviolet (NUV), visible (VIS) and very-near-infrared (350-

161   1000 nm, 8 nm spectral resolution) and a spectrometer with Indium-Gallium-Arsenide

162   linear array detector for the shortwave infrared (900-2200 nm, 12 nm resolution)

163   wavelength range. Over the entire range, about 90% of the solar irradiance spectrum is

164   captured. The slit-functions and wavelength-response of the spectrometers were

165   measured in the laboratory prior to the field experiment. An absolute radiometric

166   calibration with a National Institute of Standards and Technology (NIST) traceable light

167   source (1000 W lamp) was performed in the laboratory before and after the experiment,

168   and the stability of the calibration was monitored with field-calibrators regularly

169   throughout the experiment. The absolute radiometric accuracy was 3-5% (precision

170   0.1%). The data were corrected for the angular response of the light collectors and for

171   changes in downward irradiance due to aircraft attitude. The attitude correction was

172   necessary because the light collector reference plane (SSFR horizon) deviated from

173   horizontal alignment due to changes in aircraft pitch, roll, and heading; no active

174   stabilization as described by *Wendisch et al.* [2001] was available for this experiment. In

175   some cases, the attitude correction failed because of reflections from nearby clouds that

176   could not be accounted for by the correction algorithm.

177

178   <u>Deriving cloud absorption from SSFR measurements</u>

179   In aircraft measurements, cloud absorption is derived from the difference of net

180   irradiance, $F_{net} = F^{\downarrow} - F^{\uparrow}$, at the top and bottom of a layer: $\Delta F_{V} = F_{net,top} - F_{net,bot}$ where

181   ΔF_V denotes the vertical component of flux divergence (vertical difference of net

182   irradiance). It differs from true absorption ($F_{abs} = \Delta F = \Delta F_V + \Delta F_H$) when horizontal flux

183   divergence $\Delta F_H \neq 0$. Due to net horizontal photon transport, ΔF_H is non-zero for any

184   inhomogeneous distribution of atmospheric extinction, in particular in heterogeneous

185   clouds. It is only rarely measured directly. In absence of physical absorbers, $F_{abs} = 0$, and

186   ΔF_H is balanced by ΔF_V that is opposite in sign. The magnitude of ΔF_V is a measure for

187   net horizontal photon transport, and is called apparent absorption. For non-conservative

188   scattering, ΔF_V incorporates real absorption (F_{abs}) and net horizontal transport effects:

189    $\Delta F_V = F_{abs} - \Delta F_H$. For pronounced horizontal heterogeneity, ΔF_H may dominate ΔF_V,

190   which makes it hard to estimate F_{abs}. The reason why we focus on ΔF_V is that no

191   assumptions about cloud heterogeneity are necessary to derive it, in contrast to F_{abs}.

192

193   Fractional absorption (or apparent layer absorptance) is obtained from ΔF_V by

194   normalizing with $F^{\downarrow}_{top}$. While error analysis is virtually impossible when estimating F_{abs}

195   from ΔF_V, it is non-trivial to derive realistic error-estimates even for ΔF_V itself. A brute

196   force method would be combining the radiometric uncertainties (3-5%) with linear error

197   propagation: $e(\Delta F_V) \approx |e(F^{\downarrow}_{top})| + |e(F^{\uparrow}_{top})| + |e(F^{\downarrow}_{bot})| + |e(F^{\uparrow}_{bot})|$ where e denote systematic

198   absolute instrument uncertainties. However, since all spectrometers are calibrated with

199   the same light source, the errors are not independent. A more realistic uncertainty

200   estimate would be the stability of the spectrometer response functions throughout the

201   experiment (better than 1-2% during TC[4]). Another major contributor to total uncertainty

202   is horizontal misalignment of the sensors. Even after correcting for aircraft attitude, a

203   residual error remains. It can exceed radiometric uncertainty [*Wendisch et al.*, 2001] and

204 is hard to derive from theoretical considerations as it depends on the specific

205 measurement situation. We therefore used an empirical estimate of 7% for the maximum

206 total error in downward irradiance. This error subsumes contributions from radiometric

207 calibration, attitude correction, and angular response of the light collectors and was

208 determined by comparing downward modeled and measured irradiance above clouds and

209 in cloud-free areas for all wavelengths (excluding gas absorption bands). More detail for

210 estimating the error due to changing aircraft attitude is given in *Schmidt et al.* [2010]. For

211 the upward irradiance, we used 5% as maximum error estimate. The net-irradiance error

212 was obtained from linear error propagation: $e(F_{top}) \approx |e(F^{\downarrow}_{top})| + |e(F^{\uparrow}_{top})|$ and

213 $e(F_{bot}) \approx |e(F^{\downarrow}_{bot})| + |e(F^{\uparrow}_{bot})|$. The top-of-cloud and bottom-of-cloud errors were combined

214 by Gaussian error propagation: $e(\Delta F_V) \approx (e(F_{top})^2 + e(F_{bot})^2)^{1/2}$.

215

216 <u>MODIS Airborne Simulator</u>

217 The horizontal cloud structure was inferred from the MODIS Airborne Simulator (MAS:

218 *King et al.*, 1996). It provided fields of cloud top height, optical thickness (τ) and

219 effective cloud particle radius (r_{eff}) at a resolution between 20 and 50 m (depending on

220 flight altitude and cloud top height). For high clouds, the cloud top height retrieval was

221 based on the CO_2 slicing technique as used by MODIS [*Menzel et al.*, 2008]. The

222 algorithm that normally uses four CO_2 MODIS channels was adapted to use the three

223 channels available on MAS. However, the actual MAS cloud top properties retrieval

224 obtains realistic solutions using two CO_2 channels only. For low clouds, the algorithm

225 reverts to the IR window method. The retrieval of optical thickness and effective radius

226 was based on *Nakajima and King* [1990]: For each pixel, reflectance pairs in a visible (or

227   shortwave infrared) channel and a near-infrared channel were compared with one-

228   dimensional forward model calculations. While the shorter wavelength channel was

229   chosen outside gas absorption bands and contains mainly information on optical

230   thickness, the longer wavelength near-infrared channel is affected by liquid water or ice

231   absorption and is sensitive to drop or crystal size. The closest match of the observed

232   reflectance with pre-calculated modeled values was used to infer the optical thickness and

233   effective radius pair. For the TC[4] data processing, algorithms similar to the ones used in

234   MODIS collection 5 retrievals were used, where scattering phase functions and single

235   scattering albedo for ice clouds rely on calculations by *Baum et al.* [2005]. Liquid water

236   cloud scattering phase functions were derived from Mie calculations based on gamma

237   drop size distributions with an effective variance of 0.1 [*Platnick et al.*, 2003]. Detailed

238   instrument information and a description of the retrieval algorithm are given in King et

239   al. [2004, 2009]. *Eichler et al.* [2010] discuss the impact of crystal habit and 3D radiative

240   effects on the retrievals. MAS data collected during TC[4] were compared with MODIS

241   cloud retrievals [*King et al.*, 2010].

242

243   <u>Cloud Radar System</u>

244   The vertical cloud structure below the ER-2 flight track was derived from the reflectivity

245   profiles measured by the cloud radar system (CRS: *Li et al.,* 2004) onboard the ER-2. The

246   resolutions of the reflectivity field are 37.5 meters in the vertical and about 100 meters in

247   the horizontal. The minimum detectable reflectivity is about -28 dBZ for CRS at a

248   distance of 15 km. The reflectivity from CRS has been compared with the reflectivity

249   from another radar at X- band on the ER-2 near the cloud top. Near the cloud top, the

250   reflectivities at both radar frequencies are about the same, an indication that the ice

251   particles obey Rayleigh scattering [*Tian et al.*, 2009].

252

253   <u>Case from 17 July, 2007</u>

254   We selected one of the well-coordinated flight legs from 17 July, 2007 (from 1520 to

255   1535 UTC). Figure 1 shows this flight leg in the larger scale context (Geostationary

256   Operational Environmental Satellite (GOES) infrared image from 1528 UTC). It was

257   located 300 km south of Panama (around 5°N, 83°W), near the edge of a high-cloud

258   system. The concurrent GOES VIS image (not reproduced here) shows that the cirrus-

259   free area was partly covered by low-level clouds. The Sun azimuth was northeast, at a

260   zenith angle of approximately 35°.

261

262   Both aircraft were guided from the mission operation center at the airport in San José

263   using NASA's Real Time Mission Monitor tool (RTMM, http://rtmm.nsstc.nasa.gov/)

264   that allowed the mission manager to coordinate the aircraft within two minutes on exactly

265   the same ground track. In the 17 July case, the ER-2 and DC-8 were less than twelve

266   seconds apart on every point along the track. Despite the frequent occurrence of

267   coordinated flight legs throughout the experiment, only one case qualified for our study

268   based upon stringent selection criteria: In order to correctly quantify cloud absorption, the

269   bulk of the cloud layer had to be bracketed by the two aircraft. Due to logistical

270   constraints the DC-8 was frequently scheduled to fly only in-cloud; that is, no below-

271   cloud legs were scheduled. Even for the 17 July case studied here the DC-8 flew almost

272   entirely within the cloud layer. Since no vertical structure was available from MAS, the

273   information from CRS onboard the ER-2 was vital in order to account for the position of

274   the DC-8 within the cloud. Without this information, it would be impossible to match

275   measured and modeled irradiance at the position of the DC-8. A further, less stringent,

276   requirement was that clouds be composed entirely of ice crystals, determined by the

277   pixel-by-pixel thermodynamic phase information from MAS. Finally, only cases where

278   the attitude correction could be applied (pitch and roll angles within certain limits) were

279   used. These three requirements limited the amount of useable data considerably.

280

281   Figure 2 shows the MAS-retrieved cloud optical thickness (gridded to 500 m resolution),

282   CRS reflectivity, and the SSFR spectral albedo for the same ER-2 flight leg as in Figure

283   1. For the upper panel, blue colors correspond to low; red and black colors to high optical

284   thickness. Cloud gaps are represented by white. The length of the scene is 198 km, the

285   width (swath) 17.5 km. In Figure 2, the southeast to northwest flight track is aligned from

286   left to right. The green shaded areas in the CRS panel mark areas where no data were

287   available. The thick black line represents the MAS-derived cloud top height along the

288   ER-2 flight track which captures the cloud top structure rather well. The dotted line

289   indicates the approximate flight altitude of the DC-8, showing that during large portions

290   of the leg, the DC-8 was actually within cloud rather than below. On some sections of the

291   leg, the radar sensed low-level clouds between the surface and 4 km that were decoupled

292   from the high-level outflow of the cell northeast of the flight leg. The bottom panel shows

293   time series of spectral albedo, with the wavelength varying in the vertical. The SSFR

294   albedo is nearly saturated in the visible wavelength range (red values indicating an albedo

295   near unity) in the optically thick cloud regions. The albedo time series (horizontal lines in

13

296   the albedo panel) exhibits far less variability than the associated cloud optical thickness,

297   mainly due to the hemispherical (geometrical) averaging inherent to irradiance. Some of

298   the wavelengths show minima that correspond to gas absorption bands. Ice absorption

299   bands (for example around 1500 nm) can also be distinguished.

300

301   Table 1 shows basic statistics of the cloud field. The upper three lines show mean,

302   minimum, maximum and standard deviation of optical thickness, effective radius, and

303   cloud top height, as derived from MAS throughout the model domain. The uncertainties

304   behind the mean values are derived from the level 2 products. They are discussed more in

305   *Kindel et al.* [2010]. The lower three lines show the cloud top altitude, bottom altitude,

306   and geometrical thickness as derived from CRS along the nadir track of the ER-2 (only

307   ice cloud portion above 6 km). For comparison, the cloud top altitude along nadir as

308   derived from MAS is also shown. The mean cloud top height is 10.8 km (CRS), 10.7 km

309   (MAS, domain average), and 10.3 km (MAS, nadir track average).

310

311   <u>Input Cloud Generation</u>

312   The fields of optical thickness and effective radius from MAS and the reflectance data

313   from CRS were combined to provide the input to three-dimensional radiative transfer

314   calculations. The profile of radar reflectivity Z (in units of dBZ) was used to derive

315   approximate vertical profiles of ice water content ($IWC(z)$, in g m^{-3}) along the flight track

316   following *Liu and Illingworth* [2000]: $IWC = 0.137*Z^{0.64}$. For each vertical profile along

317   the flight track, the column-integrated ice water path (IWP_{CRS}) was calculated. The IWP

318   was also retrieved from MAS: $IWP_{MAS} = 2/3*\rho_{ice}*\tau*r_{eff}$, where ρ_{ice} is the density of ice

319   (approximately 0.925 g cm^{-3}). While the CRS profile was only measured along the center

320   (nadir) track, MAS-derived *IWP* was available across the entire swath for each point

321   along the track. In the model cloud, the *IWC* profiles were obtained through *IWC*(z) =

322   *IWC*$_{CRS}$**IWP*$_{MAS}$/*IWP*$_{CRS}$. The entire profile was shifted in altitude corresponding to the

323   cloud top height as retrieved by MAS. Due to the lack of other information, the effective

324   radius was set to r_{eff}(x,y,z)=$r_{eff,MAS}$(x,y), which is clearly a simplification because the

325   crystal size distribution in the lower regions of the cloud is fundamentally different from

326   that near the top. The MAS-derived effective radius is representative of the topmost layer

327   of the cloud [*Platnick et al.*, 2000] where ice crystals are often smaller than in lower

328   layers within the cirrus [*Francis et al.*, 1998; *Gayet et al.*, 2004]. It should be noted that

329   the MAS retrieved optical thickness is conserved by the cloud generation method, and

330   that the information from CRS is only used for the vertical distribution of extinction

331   values throughout the column. Thereby, the CRS profiles (available only below the ER-2

332   flight track) were used across the entire MAS swath. Since to first order, scattering at

333   non-absorbing wavelengths is determined by the three-dimensional distribution of cloud

334   extinction, the simplification of a vertically constant effective radius is justified in these

335   cases. For absorbing wavelengths, measurement-model discrepancies are possible

336   because absorption is a function of optical thickness and effective radius. However, a

337   considerable part of radiation is absorbed in the uppermost cloud layer. Therefore, the

338   cloud-top effective radius can be regarded as a valid representation for our study.

339

340   The generated 3D cloud was gridded to 0.5 km horizontal and 1.0 km vertical resolution.

341   The impact of spatial resolution is not the focus of this particular study; for testing, a

15

342   version with 0.1 km horizontal resolutions was also generated. Radiative transfer model

343   runs at 500 nm wavelength showed that the irradiances were hardly affected by the

344   increased horizontal resolution, and subsequently, the high-resolution cloud was not used

345   in the interest of saving CPU time. The vertical resolution of 1.0 km was chosen larger

346   than the mismatch between CRS- and MAS-derived cloud top altitude (0.5 km, see Table

347   1).

348

349   <u>Radiative Transfer Calculations</u>

350   All calculations were done with the libRadtran radiative transfer package developed by

351   *Mayer and Kylling* [2005]. The generated cloud microphysical properties within the 384

352    $\times$ 35 $\times$ 20 boxes ($n_x \times n_y \times$ number of layers) constitutes the main input for 3D RT

353   calculations, along with atmospheric profiles from dropsondes (launched from the DC-8),

354   and from the DC-8 and ER-2 meteorological data (pressure, relative humidity). For the

355   spectral sea surface albedo, data measured by SSFR during CRYSTAL-FACE (Cirrus

356   Regional Study of Tropical Anvils and Cirrus Layers – Florida Area Cirrus Experiment)

357   was used [*Schmidt et al.*, 2007b]. For the 3D RT calculations, we applied the forward

358   version of the Monte-Carlo code MYSTIC (Monte Carlo code for the physically correct

359   tracing of photons in cloudy atmospheres: *Mayer* [2009]; *Mayer* [1999]) that is embedded

360   in libRadtran (http://www.libradtran.org). The extraterrestrial spectrum by *Kurucz*

361   [1992], averaged over 1 nm bins, was used as top-of-the atmosphere incident solar

362   irradiance spectrum. For the sake of computational efficiency, the scattering phase

363   functions were represented by the Henyey-Greenstein parameterization based on the

364   asymmetry parameter *g* (the first moment of the phase function). As shown in *Schmidt et*

365 *al.* [2007b], this approximation is reasonably close to the exact representation of the

366 cloud phase function, at least for sun angles not too far from zenith position. Both

367 asymmetry parameter and single scattering albedo were taken from ray tracing

368 calculations by *Yang and Liou* [1998]. Calculations were performed for nine

369 wavelengths: 400, 450, 500, 600, 700, 800, 850, 1200, and 1600 nm, using 10^9 photons

370 each. Periodic boundary conditions were used, to ensure energy conservation in the

371 model.

372

373 3. Results

374

375 As a first step, we compared the measured time series of upward and downward

376 irradiance above (that is, at ER-2 altitude) and below (or within) clouds (that is, at DC-8

377 altitude) with model results. To this end, the downward irradiance was rescaled such that

378 changes in solar zenith angle (ranging from $SZA = 34°\text{-}36°$ during the leg) were

379 compensated using $F^\downarrow(SZA_0) = F^\downarrow(SZA) \times (\cos(SZA_0)/\cos(SZA))$, where $SZA_0 = 35°$ was

380 used in the model calculations as well. This correction is discussed in *Schmidt et al.*

381 [2007a].

382

383 Figure 3 shows the measurements and model results at DC-8 and ER-2 altitude for (a)

384 500 nm (non-absorbing wavelength), and (b) 1600 nm (absorbing wavelength). The

385 variability of the modeled downward irradiance above clouds (blue dotted lines) reflects

386 statistical (photon) noise; the variability of the measurements is due to the residual error

387 after the attitude correction, discussed in section 2. For example, the ER-2 turned at about

388   15.33 h UTC, causing a 5% drop in downward irradiance at 500 nm, and a short peak at

389   1600 nm. The empirical 7% error bar is also shown. For the ER-2 altitude (blue and red

390   lines), the model-measurement agreement is within the 7% or 5% measurement

391   uncertainties, except for the 1600 nm upwelling irradiance where the model results are

392   above the measurements. This could indicate that the effective radius in the model cloud

393   was too low, or that the measured upward irradiance was influenced by contributions

394   outside the swath of MAS which are not represented in the model. The model-

395   measurement agreement is worse at DC-8 altitude (green and magenta lines), especially

396   in areas where the cloud optical thickness is low (before 15.38 h UTC and after 15.49 h

397   UTC). There are numerous reasons for that. Firstly, within clouds, the downward and

398   upward irradiance are a strong function of altitude, and even small mismatches between

399   the vertical profile of cloud extinction (and effective radius) in the model and reality (that

400   is, the actual altitude of the DC-8) will result in large differences. Secondly, as noted

401   above, the vertical profile of cloud extinction (as derived from CRS) is only valid on the

402   nadir track (i.e. the profile between ER-2 and DC-8) and does not represent the vertical

403   cloud structure across the entire MAS swath. In some cases, cloud edge effects occur

404   only in the model results or the measurements because cloud gaps and cloud boundaries

405   are not necessarily represented realistically in the simplistic cloud algorithm.

406

407   The net irradiance is less sensitive to altitude; for wavelengths outside gas and cloud

408   absorption bands, it is expected to be constant with altitude. The vertical difference of net

409   irradiances on top and at the bottom of the cloud layer, that is, vertical flux divergence

410   (ΔF_V), is shown in Figure 4 (a: 500 nm, b: 1600 nm). At 500 nm wavelength, the clouds

411 themselves do not absorb and atmospheric gas absorption is near zero (except for the

412 ozone Chappuy band – but no signification ozone concentrations are present between the

413 altitudes of the two aircraft). No absorbing aerosol particles were present. Therefore,

414 negligible values are expected for F_{abs}. In absence of true absorption, positive values of

415 ΔF_V (apparent absorption) indicate that photons are lost through the sides of the cloud

416 column ($\Delta F_H < 0$); negative values (apparent emission) correspond to a net photon gain.

417 The observations (black dots) are shown with error bars that were estimated from the

418 individual absolute uncertainties as explained above. Throughout almost the entire leg,

419 significant apparent absorption is observed that is not balanced by negative values. On

420 average, a value of 0.17 W m^{-2} nm^{-1} is found. In the modeled vertical flux divergence, in

421 contrast, negative and positive ΔF_V values are balanced and $\langle \Delta F_V \rangle = 0$ because $F_{abs} = 0$

422 and $\langle \Delta F_H \rangle = 0$. The domain-averaged horizontal photon transport vanishes due to periodic

423 boundary conditions. Open boundary conditions could not be used because they would

424 have compromised energy conservation. The bias between observations and model varies

425 between 0 and 0.2 W m^{-2} nm^{-1}. In areas of moderate to high optical thickness (between

426 15.38 h and 15.49 h UTC), the modeled values lie within the uncertainty of the

427 observations. At some places, the discrepancies are larger than the error bars, for example

428 at UTC = 15.47 h. At this time, Figure 2 shows off-nadir track maxima of optical

429 thickness. Probably the vertical structure in these two columns was not properly captured

430 by the on-track CRS profile.

431

432 The red line shows the MAS optical thickness retrievals averaged within the SSFR

433 footprint. The SSFR footprint is usually defined as a circle from within which 50% of the

434   ER-2-measured upward irradiance originates. Table 2 shows the size of the SSFR

435   footprint diameter as a function of cloud top altitude, or cloud top to aircraft vertical

436   distance. In this case, the 50% footprint diameter is mostly contained within the model

437   domain. However, the 66% or 90% footprints are considerably larger than the MAS

438   swath. About 50% of the irradiance originates from areas that are not represented within

439   the model domain.

440

441   The limited model domain size (given by the MAS swath width) could be an explanation

442   for the discrepancy between observations and model results. While in the calculations,

443   photons are confined within the model boundaries, they are not restricted in this way in

444   the real world. If the measurement area is surrounded by regions of lower optical depth or

445   even clear sky, a net transport of photons into these regions can occur, in the same way as

446   between areas of different optical thickness *within* the domain. However, there are

447   theoretical limits for the horizontal displacement of photons. For example, the mean

448   horizontal distance traveled by transmitted photons is in the range of cloud geometrical

449   depth [*Marshak et al.*, 1995] (less for reflected photons). Although the GOES IR image

450   shows that there are indeed areas without high clouds southwest of the flight track, they

451   may be too far off to explain the observations.

452

453   For absorbing wavelengths, the root mean horizontal displacement of photons is much

454   shorter than for non-absorbing wavelengths (*Platnick et al.*, 2001; *Kassianov and Kogan*,

455   2002). It is therefore not surprising that the model-measurement discrepancy is much

456   lower for 1600 nm (Figure 4b). In addition to the modeled ΔF_V (blue circles), the green

20

457　circles show the results from the independent pixel approximation where horizontal

458　photon transport is disabled in the model. Even in areas where Figure 4a indicates strong

459　horizontal photon transport at 500 nm, the 1600 IPA model results are close to the full 3D

460　calculations. Thus, in this case, IPA provides a good estimate for true absorption. The

461　vertical position of the DC-8 within the cloud layer is of great importance for the

462　measurement-model agreement at 1600 nm. The full-column absorption of the ice cloud

463　(ΔF_V from 5 km to 20 km, magenta symbols) does not agree with the measurements

464　(column between 9 km and 20 km).

465

466　In addition to the localized radiative smoothing, irradiance fields incur hemispherical

467　(cosine-weighted) averaging of the underlying radiance fields, which could also

468　contribute to the discrepancy. After all, only about 50% of the irradiance originates from

469　within the MAS swath, and the model results can be biased if the clouds outside the

470　domain are not properly represented by the model cloud. Both effects – photon loss into

471　neighboring areas and geometrical averaging – can only be examined by embedding the

472　MAS-based cloud within the larger context of GOES-derived cloud fields. This is beyond

473　the scope of this study. Until radiative transfer calculations in an extended domain prove

474　the explanations brought forward, one cannot rule out other causes for the discrepancies.

475

476　Figure 5 illustrates the relationship between cloud optical thickness and ΔF_V. The

477　observations are shown for 500 nm (black dots) and 1600 nm (red dots), as a function of

478　MAS-retrieved optical thickness (averaged over the SSFR footprint). The propagated

479　error from the measurement uncertainties is shown at maximum optical thickness. The

480   error is larger for 500 nm (only negative error bar is shown) than for 1600 nm because

481   500 nm is near the maximum of the solar spectrum, and ΔF_V is derived from the

482   difference of large (500 nm) as opposed to small (1600 nm) quantities. In this particular

483   case, the values of ΔF_V are comparable in magnitude for the two wavelengths although

484   the processes involved are fundamentally different: At 1600 nm, true absorption by ice

485   crystals prevails. The modeled dependence of F_{abs} on optical thickness a red line.

486   Observed (small) excursions from the modeled values can be explained by horizontal

487   photon transport: $\Delta F_V = F_{abs} - \Delta F_H$. At 500 nm, in contrast, the true absorption is

488   expected to be close to zero ($F_{abs} \approx 0$), and $\Delta F_V \approx -\Delta F_H$. As discussed before, almost all

489   the observations exhibit positive ΔF_V, whereas the values from the 3D model calculations

490   (blue dots) do not show such a bias.

491

492   There is some indication from the model and observations that net transport of radiation

493   occurs from optically thicker to thinner regions. Obviously no 1:1 relationship can be

494   established, partly because net photon transport takes place between *local* maxima and

495   minima of optical thickness. Net transport of radiation is not induced by optical thickness

496   contrasts if they are separated by scales larger than the mean horizontal photon

497   displacement. For example, radiative smoothing, and thus ΔF_H, at 1600 nm is suppressed

498   in comparison to 500 nm because the absorption has a shortening effect on photon

499   horizontal transport distances.

500   For small optical thickness (5-13 in Figure 5), positive and negative apparent absorption

501   occurs in the model calculations, uncorrelated with the optical thickness itself. These

502   excursions from zero absorption suggest that in areas with sparse or thin cloud cover,

503   other factors than large-scale horizontal cloud distribution dominate photon transport, for

504   example vertical heterogeneities (multiple layers) and interactions with the surface.

505

506   Figure 6 shows the time series of the measurement-derived apparent absorptance (defined

507   as $\Delta F_V / F^{\downarrow}_{top} \times 100\%$) at four conservative, and one absorbing wavelength. Along most of

508   the leg, the apparent absorptance increases as a function of wavelength. This is further

509   analyzed in Figure 7 where we show the spectral shape of measurement-derived and

510   simulated apparent cloud absorptance in two different areas of the cloud: at UTC = 15.38

511   h (local maximum of τ – red line) and at UTC = 15.44 h (local minimum of τ – blue

512   line), both of which are marked in Figures 4 and 6. Results from the 3D model runs are

513   shown as red and blue symbols. The black line shows the absorptance spectrum obtained

514   when averaging observations over the entire leg from UTC=15.33 h – 15.53 h. In the

515   visible and very-near-infrared wavelength area, the leg-averaged spectrum is close to the

516   high optical thickness case (blue spectrum); at near-infrared wavelengths, it is closer to

517   the low optical depth case (red spectrum). The measured broadband apparent absorption

518   is 185 W m^{-2} (leg-averaged), 221 W m^{-2} (optically thick case), and 115 W m^{-2} (optically

519   thin case). The black dashed line shows the absorptance spectrum from a 1D calculation

520   where the optical thickness and effective radius input were obtained from averaging the

521   properties throughout the model domain. It shows that true absorption starts only between

522   1000 nm and 1200 nm where the single scattering albedo drops below unity [Kindel et

523   al., 2010, Figure 1]. The 1D modeled broadband-integrated value is 100 W m^{-2}, whereof

524   only 9 W m^{-2} occur below 1000 nm. The measured leg-averaged apparent absorption is

525   composed of 88 W m^{-2} below and 97 W m^{-2} above 1000 nm. Above 1000 nm, the

526   measured value (97 W m^{-2}) is only slightly higher than modeled (91 Wm^{-2}). In ice

527   absorption bands (e.g., 1500 nm), the spectral measurements (solid black line) are slightly

528   lower than modeled (dashed line). Below 1000 nm, the disagreement between measured

529   apparent absorption (88 W m^{-2}) and 1D modeled (true) absorption (9 W m^{-2}) is much

530   greater. The 9 W m^{-2} true absorption are caused by gas absorption, for example from the

531   oxygen A-band around 762 nm, or water vapor absorption at 940 nm, 1140 nm and 1350

532   nm (clearly visible in Figure 7). The water vapor absorption is rather weak because at

533   high altitudes, water vapor concentration is low. Subtracting the 9 W m^{-2} of gas

534   absorption from the measured value of 88 W m^{-2} leaves 79 W m^{-2} that are unaccounted

535   for by the 1D model.

536

537   Analyzing the reasons behind this is achieved by resorting to spectral and temporal

538   resolution: The measured and 3D-modeled absorptance spectra on a point-by-point basis

539   (optically thin and thick case) show considerable apparent absorption (5-15%) all across

540   the visible wavelength range, with an upward slope at wavelengths short of 450 nm. For

541   the higher optical thickness case (15.38 h), the spectral behavior is reproduced by the 3D

542   calculations (blue circles), although not equally across the spectrum (for example, 800

543   and 850 nm). This gives us some confidence that the observed effects are not

544   measurement artifacts. Above 500 nm, the range of uncertainty of absorptance excludes

545   zero, and the apparent absorption effect is statistically significant. For the low optical

546   thickness case (15.44 h), the 3D model predicts near-zero apparent absorption across

547   most of the visible range while the measured spectrum shows value of up to 10%. At

548   1200 nm, the measurement error bar only marginally contains the modeled near-zero

549   apparent absorption. Overall, there is some indication that even the 3D model

550   underestimates the measured apparent absorption (especially in optically thin areas).

551

552   The reason for the spectral slope at the shortest wavelengths is not entirely understood. It

553   is likely due to the wavelength-dependence of horizontal photon transport. *Marshak et al.*

554   [2008] described a related effect for radiance, the so-called "bluing of the atmosphere"

555   around clouds. Since molecular scattering is stronger at short wavelengths, enhanced

556   reflected radiation near cloud edges gets scattered more effectively at short ("blue")

557   wavelengths and is redirected into satellite sensors. *Redemann et al.* [2009] describe a

558   "reddening" of the atmosphere, caused by a combination of molecular scattering and

559   aerosol scattering in the vicinity of clouds. Preliminary tests showed that switching off

560   molecular scattering in the RT model did not change the slope significantly, thus ruling

561   out molecular scattering as a cause for the spectral slope of the apparent absorptance.

562

563   The spectral signature of the apparent absorption may prove important for cloud and

564   aerosol remote sensing. If the reflectance at different wavelengths responds differently to

565   cloud heterogeneity effects, this has consequences for cloud retrievals. This spectral

566   aspect of cloud retrieval biases occurs in addition to various 3D effects that have been

567   discussed in the literature. Due to the different spatial scales, this additional effect may be

568   more important for cirrus than for boundary layer clouds. A further implication is that

569   any retrieval based on reflectance ratios in the near-UV and visible wavelength range,

570   such as the aerosol index, will be distorted in the presence of cirrus, or other clouds.

571   Regarding the correction technique of *Ackerman and Cox* [1981], the visible wavelength

572   for correcting net horizontal photon transport in absorption measurements needs to be

573   chosen carefully, since the strength of horizontal photon transport varies throughout the

574   non-absorbing part of the spectrum.

575

576   ## 4. Conclusions

577

578   In this paper, we studied measured and modeled solar spectral absorption, based on data

579   from the NASA TC^4 experiment in Costa Rica (2007). Most previous studies sought to

580   infer true absorption F_{abs} from measurements of vertical flux divergence. This is

581   problematic in heterogeneous clouds where horizontal fluxes occur. Therefore, we

582   focused on apparent cloud absorption (vertical flux divergence ΔF_V), a quantity that

583   comprises net horizontal photon transport (horizontal flux divergence ΔF_H) as well as

584   true cloud absorption, F_{abs}: $\Delta F_V = F_{abs} - \Delta F_H$. We used SSFR measurements of upward

585   and downward spectral solar irradiance onboard the NASA ER-2 and DC-8 aircraft that

586   were flown in stacked formation above and below the outflow of a tropical convective

587   system on the 17 July, 2007. NASA's aircraft-ground communication tool (RTMM)

588   allowed a close coordination of the two aircraft in time and space. In this way, the cloud

589   field was sampled over more than 192 km, and a time series of apparent absorption was

590   derived from the differences of above and below-cloud net irradiances. In addition,

591   simultaneous cloud remote-sensing data (MAS-derived horizontal distribution of cloud

592   optical thickness, crystal effective radius, and cloud top height, as well as CRS-derived

593   cloud extinction profiles) were available from the high-flying aircraft. This allowed

594   generating a 3D model cloud that could be used as input to 3D radiative transfer

595   calculations to validate the measurements on a point-by-point basis along the entire flight

596   leg. The spectrally-resolved point-by-point approach allows understanding the effects of

597   horizontal photon transport in more detail than previously possible: For the first time, we

598   were able to determine the spectral shape of the vertical net flux difference (apparent

599   absorption), and to reproduce it with model calculations. We found considerable positive

600   apparent absorption in the visible wavelength range where clouds do not absorb ($F_{abs} = 0$)

601   that could, at least in part, be explained by net horizontal photon transport. Below 500

602   nm, the apparent absorption decreases with wavelength and can become negative, thus

603   entailing apparent emission of blue to near-UV radiation by clouds. The effective radius

604   in the model may have been slightly underestimated, but major adjustments of the

605   effective radius like in *O'Hirok and Gautier* [2003] were not required to achieve model-

606   measurement agreement in the true absorption. For non-absorbing wavelengths,

607   measured apparent absorption exceeded 3D model calculations at various points along

608   the leg and averaged over the entire leg. The GOES-IR image indicates that the sampled

609   cloud field was surrounded by areas of lower optical thickness or cirrus-free sky which

610   could give rise to a net loss of photons from the sample area (unaccounted for by the

611   model), thus explaining the enhanced value of apparent absorption in the observations. It

612   was, however, beyond the scope of this study to explore if including the areas around the

613   sample cloud in the model calculations would support this hypothesis and thus fully

614   resolve the reasons for previously observed "absorption bias".

615

616   The bias between measured leg-averaged apparent absorption below 1000 nm (88 W m^{-2})

617   and the 1D-modeled value (9 W m^{-2}) is only partially resolved by looking at the spectral

618 and spatial (temporal) details: While 3D calculations of apparent absorptance are in

619 agreement with the measurements in optically thick regions, there is some indication that

620 even the 3D model underestimates the apparent absorption in optically thin regions,

621 which could be explained by the hypothesized net photon loss into the surrounding

622 regions (not included in the 3D model domain) that have even lower optical depth.

623

624 An open question is over which scales photons can effectively be transported within

625 clouds, or away from cloud systems into clear-sky areas. For boundary layer clouds,

626 theoretical limits exist for the root mean horizontal photon displacement [*Platnick*, 2001].

627 On average, the geometrical distance does not exceed the vertical extent of a cloud layer

628 [*Marshak et al.*, 1995]. When sampling clouds over areas that are larger than this

629 distance, the net horizontal photon flux is expected to be balanced ($\langle\Delta F_\mathrm{H}\rangle = 0$). Those

630 distances might be larger in high-cloud systems, especially when multiple layers are

631 involved. Moreover, the geometrical averaging inherent to irradiance introduces different

632 effects for boundary layer clouds and large-scale convection systems, just because of the

633 different dimensions. *Kindel et al.* [2009] (Figure 11) shows that irradiance-based

634 retrievals of cloud optical properties of anvils are biased low with respect to radiance-

635 based counterparts, because of the influence of clear-sky areas beyond the imager's

636 swath.

637

638 A different manifestation of net horizontal photon transport was observed by *Eichler et*

639 *al.* [2010], using the same model cloud as employed in this study. The net outflow of

640 photons from optically thick areas makes them appear darker and leads to an

641 underestimation of cloud optical thickness by the imager. The opposite effect in optically

642 thin areas does not fully compensate this bias and leads to a net effect of underestimation

643 of optical thickness. As shown above, this effect is not spectrally neutral. Remote sensing

644 techniques that rely on reflectance ratios at different wavelengths such as the aerosol

645 index will thus be heavily affected in the presence of clouds.

646

647 The physical basis of the spectral shape of near-UV and visible apparent absorption

648 remains to be explored, as well as the scales over which horizontal photon transport

649 occurs in high cloud systems (for example, by embedding the MAS cloud scene in the

650 larger context of GOES retrievals). New measurement techniques such as a payload that

651 can be lowered down into and below a cloud from an aircraft [*Frey et al.*, 2009] will

652 make apparent absorption measurements easier and provide a link with cloud

653 microphysics.

654

655 ## Acknowledgements

664   as a guest scientist at the Meteorological Institute of the University for Natural Resources

665   and Applied Life Sciences in Vienna. Thanks to the colleagues in Austria for their

666   hospitality and discussions.

667

668   <u>References</u>

669   Ackerman, S. A., and G. L. Stephens (1987), The absorption of shortwave solar radiation

670   by cloud droplets: an application of anomalous diffraction theory. *J. Atmos. Sci.*, *44*,

671   1574-1588.

672

673   Ackerman, S. A., and S. K. Cox (1981), Aircraft observations of shortwave fractional

674   absorptance of non-homogeneous clouds, *J. Appl. Meteorol.*, *20*, 1510-1515.

675

676   Ackerman, T. P., D. M. Flynn, and R. T. Marchand (2003), Quantifying the magnitude of

677   anomalous solar absorption, *J. Geophys. Res.*, *109*(D9), 4273.

678

679   Arking, A. (1999), The influence of clouds and water vapor on atmospheric absorption,

680   *Geophys. Res. Lett.*, *26*, 2729-2732.

681

682   Arking, A. (1996), Absorption of solar energy in the atmosphere: Discrepancy between

683   model and observations, *Science*, *273*, 779-782.

684

685   Baum, B. A., A. J. Heymsfield, P. Yang, and S. T. Bedka (2005), Bulk scattering

686   properties for the remote sensing of ice clouds. Part I: Microphysical data and models, *J.*

687   *Appl. Meteor.*, *44*, 1885–1895.

688

689   Cess, R. D., M. H. Zhang, P. Minnis, L. Corsetti, E. G. Dutton, B. W. Forgan, D. P.

690   Garber, W. L. Gates, J. J. Hack, E. F. Harrison, X. Jing, J. T. Kiehl, C. N. Long, J. J.

691   Morcrette, G. L. Potter, V. Ramanathan, B. Subasilar, C. H. Whitlock, D. F. Yound, and

692   Y. Zhou (1995), Absorption of solar radiation by clouds: Observations versus models,

693   *Science*, *267*, 496-499.

694

695   Chylek, P., G. B. Lesins, G. Videen, J. G. D. Wong, R. G. Pinnick, D. Ngo, and J. D.

696   Klett (1996), Black carbon an absorption of solar radiation by clouds, *J. Geophys. Res.*,

697   *101*, 23365-23371.

698

699   Chylek, P., V. Ramaswamy, and R. J. Cheng (1984), Effect of graphitic carbon on the

700   albedo of clouds, *J. Atmos. Sci.*, *41*, 3076-3084.

701

702   Davis, A. B., and A. Marshak (2001), Multiple scattering in clouds: Insights from three-

703   dimensional diffusion/P1 theory, *Nuclear Science Engineer.*, *136*, 251-280.

704

705   Eichler, H., K. S. Schmidt, R. Buras, M. Wendisch, B. Mayer, P. Pilewskie, M. King, L.

706   Tian, G. Heymsfield, S. Platnick (2010), Cirrus spatial heterogeneity and ice crystal

707 shape: Effects on remote sensing of cirrus optical thickness and effective crystal radius,

708 *submitted to J. Geophys. Res*.

709

710 Francis, P., P. Hignett, A. Macke (1998), The retrieval of cirrus cloud properties from

711 aircraft multi-spectral reflectance measurements during EUCREX '93, *Q. J. R. Meteorol.*

712 *Soc., 124*, 1273-1291.

713

714 Francis, P. N., J. P. Taylor, P. Hignett, and A. Slingo (1997), On the question of

715 enhanced absorption of solar radiation by clouds, *Q. J. R. Meteorol. Soc.*, *123*, 419-434.

716

717 Frey, W., H. Eichler, M. de Reus, R. Maser, M. Wendisch, and S. Borrmann (2009), A

718 new airborne tandem platform for collocated measurements of microphysical cloud and

719 radiation properties, *Atmos. Meas. Tech., 2*, 147-158.

720

721 Kassianov, E. I., and Y. L. Kogan (2002), Spectral dependence of radiative horizontal

722 transport in stratocumulus clouds and its effect on near-IR absorption, J. Geophys. Res.,

723 107(D23), 4712, doi:10.1029/2002JD002103.

724 Redemann, Jens, Qin Zhang, Philip B. Russell, John M. Livingston, and Lorraine A.

725 Remer (2009), Case studies of aerosol remote sensing in the vicinity of clouds, J Geophys

726 Res, 114, D06209.

727

728 Fritz, S., and T. H. MacDonald (1951), Measurements of absorption of solar radiation by

729 clouds, *Bull. Amer. Meteorol. Soc.*, *32*, 205-209.

730

731   Gayet, J. F., J. Ovarlez, V. Shcherbakov, J. Strom, U. Schumann, A. Minikin, F. Auriol,

732   A. Petzold, M. Monier (2004), Cirrus cloud microphysical and optical properties at

733   southern and northern midlatitudes during the INCA experiment, *J. Geophys. Res., 109*,

734   D20206.

735

736   Harshvardhan, W. Ridgway, V. Ramaswamy, S.M. Freidenreich, M. Batey (1998),

737   Spectral Characteristics of Solar Near-Infrared Absorption in Cloudy Atmospheres. *J.*

738   *Geophys. Res., 103*, D22, 28793-28799.

739

740   Hayasaka, T., N. Kikuchi, and M. Tanaka (1995), Absorption of solar radiation by

741   stratocumulus clouds: Aircraft measurements and theoretical calculations, *J. Appl.*

742   *Meteorol.*, *34*, 1047-1055.

743

744   Kassianov, E. I., and Y. L. Kogan (2002), Spectral dependence of radiative horizontal

745   transport in stratocumulus clouds and its effect on near-IR absorption, *J. Geophys. Res.*,

746   *107*(D23), 4712, doi:10.1029/2002JD002103.

747

748   Kindel, B. C., K. S. Schmidt, P. Pilewskie, B. Baum, P. Yang, S. Platnick (2009),

749   Observations and modeling of cirrus shortwave spectral albedo during the Tropical

750   Composition, Cloud and Climate Coupling Experiment, *accepted for J. Geophys. Res.*,

751   this special issue.

752

753   King, M. D., M. G. Strange, P. Leone, and L. R. Blaine (1986) Multiwavelength scanning

754   radiometer for airborne measurements of scattered radiation within clouds, *J. Atmos.*

755   *Oceanic Technol., 3*, 513-522.

756

757   King, M. D., L. F. Radke, and P. V. Hobbs (1990) Determination of the spectral

758   absorption of solar radiation by marine stratocumulus clouds from airborne

759   measurements within clouds, *J. Atmos. Sci.*, *47*, 894-907.

760

761   King, M. D, W. P. Menzel, P. S. Grant, J. S. Myers, G. T. Arnold, S. E. Platnick, L. E.

762   Gumley, S. C. Tsay, C. C. Moeller, M. Fitzgerald, K. S. Brown, and F. G. Osterwisch

763   (1996), Airborne scanning spectrometer for remote sensing of cloud, aerosol, water vapor

764   and surface properties, *J. Atmos. Oceanic Technol.*, *13*, 777-794.

765

766   King, M. D., S. Platnick, G. Wind, G. T. Arnold, and R. T. Dominguez (2010), Remote

767   sensing of radiative and microphysical properties of clouds during TC[4]: Results from

768   MAS, MASTER, MODIS, and MISR, submitted to *J. Geophys. Res.*, this special issue.

769

770   King, M. D., S. Platnick, P. Yang, G. T. Arnold, M. A. Gray, J. C. Riedi, S. A.

771   Ackerman, K. N. Liou (2004), Remote sensing of liquid water and ice cloud optical

772   thickness and effective radius in the Arctic: Application of airborne multispectral MAS

773   data*, J. Atmos. Oceanic Technol.*, *21* (6), 857–875.

774

775 Knyazikhin, Y., A. Marshak, W. J. Wiscombe, J. V. Martonchik, and R. B. Myneni

776 (2002), A missing solution to the transport equation and its effect on estimation of cloud

777 absorptive properties, *J. Atmos Sci.*, *59*, 3572-3585.

778

779 Kurucz, R. L. (1992), Synthetic Infrared Spectra, in Infrared solar physics: proceedings

780 of the 154th Symposium of the International Astronomical Union, edited by D. M. Rabin,

781 J. T. Jefferies, and C. Lindsey, Kluwer Academic Publishers, Dordrecht, the Netherlands,

782 523-531.

783

784 Liu, C., and A. Illingworth (2000), Toward more accurate retrievals of ice water content

785 from radar measurements of clouds, *J. Appl. Meteorol., 39*, 1130-1146.

786

787 Li, L., G. M. Heymsfield, P. E. Racette, L. Tian, and E. Zenker (2004), A 94 GHz cloud

788 radar system on a NASA high-altitude ER-2 aircraft, *J. Atmos. Ocean. Technol.*, *21*,

789 1378-1388.

790

791 Marshak, A., G. Wen, J. Coakley, L. Remer, N. G. Loeb, and R. F. Cahalan (2008), A

792 simple model for the cloud adjacency effect and the apparent bluing of aerosols near

793 clouds. *J. Geophys. Res.*, *113*, D14S17, doi:10.1029/2007JD009196.

794

795 Marshak, A., S. Platnick, T. Varnai, G. Wen, and R. F. Cahalan (2006), Impact of three-

796 dimensional radiative effects on satellite retrievals of cloud droplet sizes, *J. Geophys.*

797 *Res.*, *111*(D09207), doi10.1029/2005JD006686.

798

799   Marshak, A., W. Wiscombe, A. Davis, L. Oreopoulos, R. Cahalan (1999), On the

800   removal of the effect of horizontal fluxes in two-aircraft measurements of cloud

801   absorption, *Q. J. R. Meteorol. Soc.*, *125*, 2153-2170

802   .

803   Marshak, A., A. Davis, W. J. Wiscombe, W. Ridgway, and R. Cahalan (1998), Biases in

804   shortwave column absorption in the presence of fractal clouds, *J. Climate*, *11*, 431-446.

805

806   Marshak, A., A. Davis, W. Wiscombe, and R. Cahalan (1997), Inhomogeneity effects on

807   cloud shortwave absorption measurement: Two-aircraft simulations, *J. Geophys. Res.*,

808   *102*, 16619-16637.

809

810   Marshak, A., A. Davis, W. Wiscombe, and R. Cahalan (1995), Radiative smoothing in

811   fractal clouds, *J. Geophys. Res.*, *100*(D12), 26247-26261.

812

813   Mayer, B. (2009), Radiative transfer in the cloudy atmosphere, *The European Physical*

814   *Journal Conferences, 1*, 75-99.

815

816   Mayer, B., A. Kylling (2005), Technical note: The libRadtran software package for

817   radiative transfer calculations - description and examples of use, *Atmos. Chem. Phys., 5*,

818   1855-1877.

819

820   Mayer, B. (1999), 'I3RC phase 1 results from the MYSTIC Monte Carlo 384 model,

821   paper presented at the I3RC Workshop, NASA, Tucson, Ariz.

822

823   Menzel, W. P., R. Frey, H. Zhang, D. Wylie, C. Moeller, R. Holz, B. Maddux, B. A.

824   Baum, K. Strabala, and L. Gumley (2008) MODIS global cloud-top pressure and amount

825   estimation: algorithm description and results. *J. Appl. Meteor. Clim.*, *47*, 1175-1198.

826

827   Nakajima, T., and M. King (1990), Determination of the optical thickness and effective

828   particle radius of clouds from reflected solar radiation measurements. Part I: Theory, *J.*

829   *Atmos. Sci.*, *47*, 1878–1893.

830

831   Newiger, M., and Baehnke, K. (1981), Influence of cloud composition and cloud

832   geometry on the absorption of solar radiation, *Contrib. Atmos. Phys.*, *54*, 370-382.

833

834   O'Hirok, W., and C. Gautier (2003), Absorption of shortwave radiation in a cloudy

835   atmosphere: Observed and theoretical estimates during the second Atmospheric

836   Radiation Measurement Enhanced Shortwave Experiment (ARESE), *J. Geophys. Res.*,

837   *108*(D14), doi:10.1029/2002JD002818.

838

839   O'Hirok, W., C. Gautier, and P. Ricchiazzi (2000), Spectral signature of column solar

840   radiation absorption during the Atmospheric Radiation Measurement Enhanced

841   Shortwave Experiment (ARESE), *J. Geophys. Res.*, *105*(D13), 17471-17480.

842

843   Pilewskie, P., J. Pommier, R. Bergstrom, W. Gore, S. Howard, M. Rabbette, B. Schmid,

844   P. V. Hobbs, and S. C. Tsay (2003), Solar spectral radiative forcing during the Southern

845   African Regional Science Initiative, *J. Geophys. Res.*, *108*(D13), 8486,

846   doi:10.1029/2002JD002411.

847

848   Pilewskie, P., and F. P. J. Valero (1996), Response to 'How much solar radiation do

849   clouds absorb?' by G. L. Stephens, *Science*, *271*, 1134-1134.

850

851   Pilewskie, P., and F. P. J. Valero (1995), Direct observations of excess solar absorption

852   by clouds, *Science*, **267**, 1626-1629.

853

854   Platnick, S., M. D. King, S. A. Ackerman, W. P. Menzel, B. A. Baum, J. C. Riedi, and R.

855   A. Frey (2003), The MODIS cloud products: Algorithms and examples from Terra, *IEEE*

856   *Trans. Geosci. Remote Sens.*, *41*, 459–473.

857

858   Platnick, S. (2001), Approximations for horizontal photon transport in cloud remote

859   sensing problems, *J. Quant. Spectrosc. Radiat. Transfer*, *68*, 75-99.

860

861   Platnick, S. (2000), Vertical photon transport in cloud remote sensing problems, *J.*

862   *Geophys. Res.*, *105*, 22919-22935.

863

864   Ramanathan, V., B. Subasilar, G. J. Zhang, W. Conant, R. D. Cess, J. T. Kiehl, H. Grassl,

865   and L. Shi (1995), Warm pool heat budget and shortwave cloud forcing: A missing

866   physics?, *Science*, *267*, 499-503.

867

868   Rawlins, F. (1989), Aircraft measurements of the solar absorption by broken cloud fields:

869   A case study, *Quart. J. Royal Meteorol. Soc.*, *115*, 365-382.

870

871   Redemann, J., Q. Zhang, P. B. Russell, J. M. Livingston, and L. A. Remer (2009), Case

872   studies of aerosol remote sensing in the vicinity of clouds, *J. Geophys. Res.*, *114*,

873   D06209.

874

875   Schmidt, K. S., V. Venema, F. Di Giuseppe, R. Scheirer, M. Wendisch, and P. Pilewski

876   (2007): Reproducing cloud microphysical and irradiance measurements using three 3D

877   cloud generators. *Q. J. R. Meteorol. Soc.*, *133*, 765-780.

878

879   Schmidt, K. S., P. Pilewskie, S. Platnick, G. Wind, P. Yang, and M. Wendisch (2007b),

880   Comparing irradiance fields derived from Moderate Resolution Imaging

881   Spectroradiometer airborne simulator cirrus cloud retrievals with solar spectral flux

882   radiometer measurements, *J. Geophys. Res.*, *112*, D24206, doi:10.1029/2007JD008711.

883

884   Schmidt, K. S., P. Pilewskie, R. Bergstrom, O. Coddington, J. Redemann, J. Livingston,

885   P. Russell, E. Bierwirth, M. Wendisch, W. Gore, M. K. Dubey, and C. Mazzoleni, 2010,

886   A new method for deriving aerosol solar radiative forcing and its first application within

887   MILAGRO/INTEX-B, accepted for *ACP Discussions*.

888

889   Stephens, G. L. (1996), How much solar radiation do clouds absorb?, *Science*, *271*, 1131-

890   1133.

891

892   Stephens, G. L., and S. Tsay (1990), On the cloud absorption anomaly, *Q. J. R. Meteorol.*

893   *Soc.*, *116*, 671-704.

894

895   Taylor, J. P., J. M. Edwards, M. D. Glew, P. Hignett, and A. Slingo (1996), Studies with

896   a flexible new radiation code. II: Comparison with aircraft short-wave observations, *Q. J.*

897   *R. Meteorol. Soc.*, *122*, 839-861.

898

899   Tian, L., G. M. Heymsfield, A. J. Heymsfield, A. Bansemer, L. Li, C. H. Twohy, and R.

900   C. Srivastava (2009), A study of cirrus ice particle size distribution using TC[4]

901   observations, *J. Atmos. Sci.*, in press.

902

903   Titov, G. A. (1998), Radiative horizontal transport and absorption in stratocumulus

904   clouds, *J. Atmos. Res.*, *55*, 2549-2560.

905

906   Toon, O. B., D. Starr, E. Jensen, Jucks, M. Kurylo, H. Maring, P. Newman, S. Platnick,

907   M. Schoeberl, P. Wennberg, Wofsy (2009), The planning and execution of TC4,

908   submitted to *J. Geophys. Res.*, this special issue.

909

910 Valero, F. P. J., P. Minnis, S. K. Pope, A. Bucholtz, B. C. Bush, D. R. Doelling, W. L.

911 Smith Jr., and X. Dong (2000), Absorption of solar radiation by the atmosphere as

912 determined using satellite, aircraft, and surface data during the Atmospheric Radiation

913 Measurements Enhanced Shortwave Experiment (ARESE), *J. Geophys. Res.*, *105*, 4743-

914 4758.

915

916 Valero, F. P. J., R. D. Cess, M. Zhang, S. K. Pope, A. Bucholtz, B. Bush, and J. Vitko, Jr.

917 (1997), Absorption of solar radiation by the cloudy atmosphere: Interpretations of

918 collocated aircraft instruments, *J. Geophys. Res*., *102*, 29917-29927.

919

920 Wendisch, M., D. Müller, D. Schell, and J. Heintzenberg (2001), An airborne spectral

921 albedometer with active horizontal stabilization, *J. Atmos. Oceanic Technol.*, *18*, 1856-

922 1866.

923

924 Wendisch, M., and A. Keil (1999), Discrepancies between measured and modeled solar

925 and UV radiation within polluted boundary layer clouds, *J. Geophys. Res.*, *104*, 27373-

926 27385.

927

928 Wiscombe, W. J., R. M. Welch, and W. D. Hall (1984), The effects of very large drops

929 on cloud absorption, Part I: parcel models, *J. Atmos. Sci.*, *41*, 1336-1355.

930

931   Yang, P., and K. N. Liou (1998), Single-scattering properties of complex ice crystals in

932   terrestrial atmosphere, *Contr. Atmos. Physics*, *71*, 223-248.

933

934   Zhang, M., R. D. Cess, and X. Jing (1997), Concerning the interpretation of enhanced

935   cloud shortwave absorption using monthly-mean Earth Radiation Budget

936   Experiment/Global Energy Balance Archive measurement, *J. Geophys. Res.*, *102*, 25899-

937   25905.

938

939   Zinner, T., and B. Mayer (2006), Remote sensing of stratocumulus clouds: Uncertainties

940   and biases due to inhomogeneity, *J. Geophys. Res.*, *111*, D14209,

941   doi:10.1029/2005JD006955.

942

943 **Table 1 –** Statistical properties of the cloud measured on July 17, 2007, from MAS (domain, or along nadir

944 track) and CRS (along track nadir only). The quantities marked with an asterisk are discussed by *Kindel et*

945 *al.* [2010].

	mean	standard deviation	minimum	maximum
Optical Thickness (domain)	$12.5\pm2.5^*$	5.5^*	3.5	100.0
Effective Radius [μm] (domain)	$27.5\pm2.8^*$	4.6^*	4.1	42.8
Cloud Top MAS [km] (domain)	10.7	0.8	8.2	12.6
(track)	10.3	0.9	8.4	11.8
Cloud Top CRS [km] (track)	10.8	1.3	7.6	12.6
Cloud Bottom CRS [km] (track)	7.5	1.0	6.5	11.5
Geometrical Thickness CRS [km]	3.3	1.5	0.0	5.6

946

947

948 **Table 2 –** Footprint diameter for an aircraft altitude of 20 km, for several cloud top heights, and

949 corresponding aircraft-cloud top distances. The percentage in the first column indicates the fraction of

950 upward irradiance originating from within the footprint diameter; the angle in the last column is the

951 corresponding cone opening angle.

Cloud Top [km]	8.0	10.0	13.0			
AC-Cloud [km]	12.0	10.0	7.0	2.0	1.0	
Irradiance Ratio						Cone Angle [°]
33%	16.8	14.0	9.8	2.8	1.4	35
50%	24.0	20.0	14.0	4.0	2.0	45
66%	33.4	27.9	19.5	5.6	2.8	54
90%	72.0	60.0	42.0	12.0	6.0	72

952

953

954

955
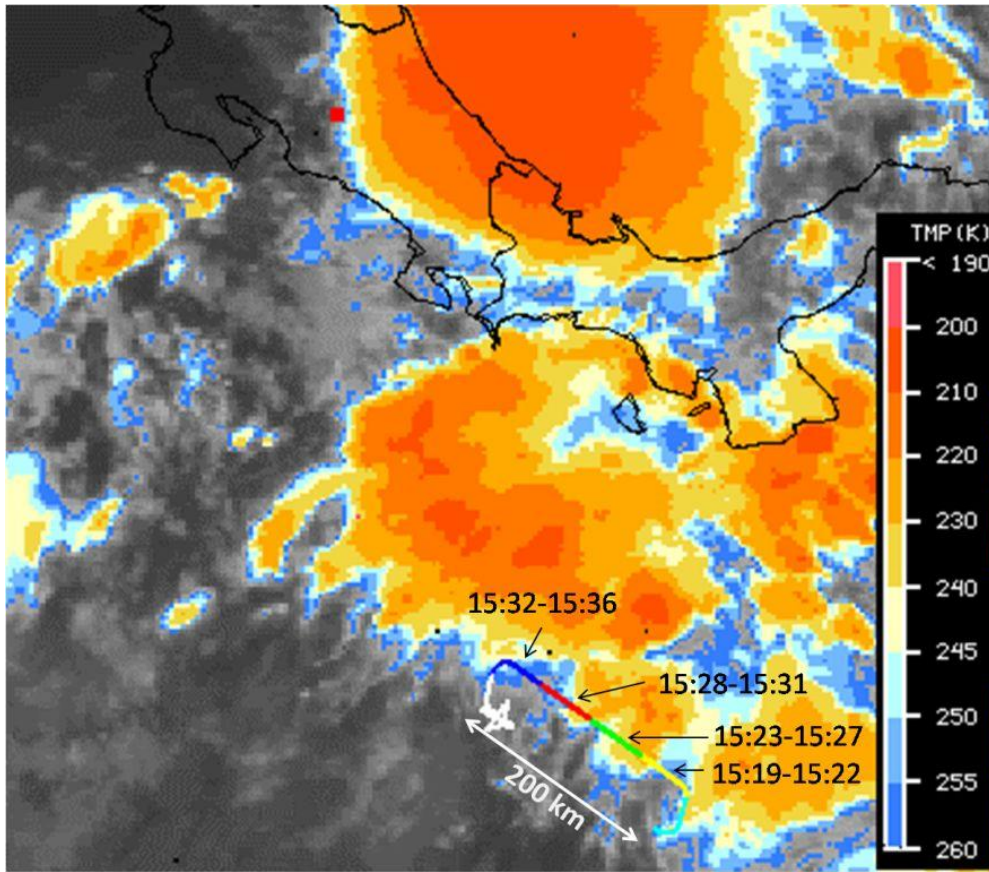
Figure 1 – ER-2 flight leg from 1519 to 1536 UTC, in the context of the GOES 10 and 12 IR image from 1528 UTC. The DC-8 was flown directly underneath. Image courtesy NASA Langley Research Center (http://www-angler.larc.nasa.gov/tc4/)
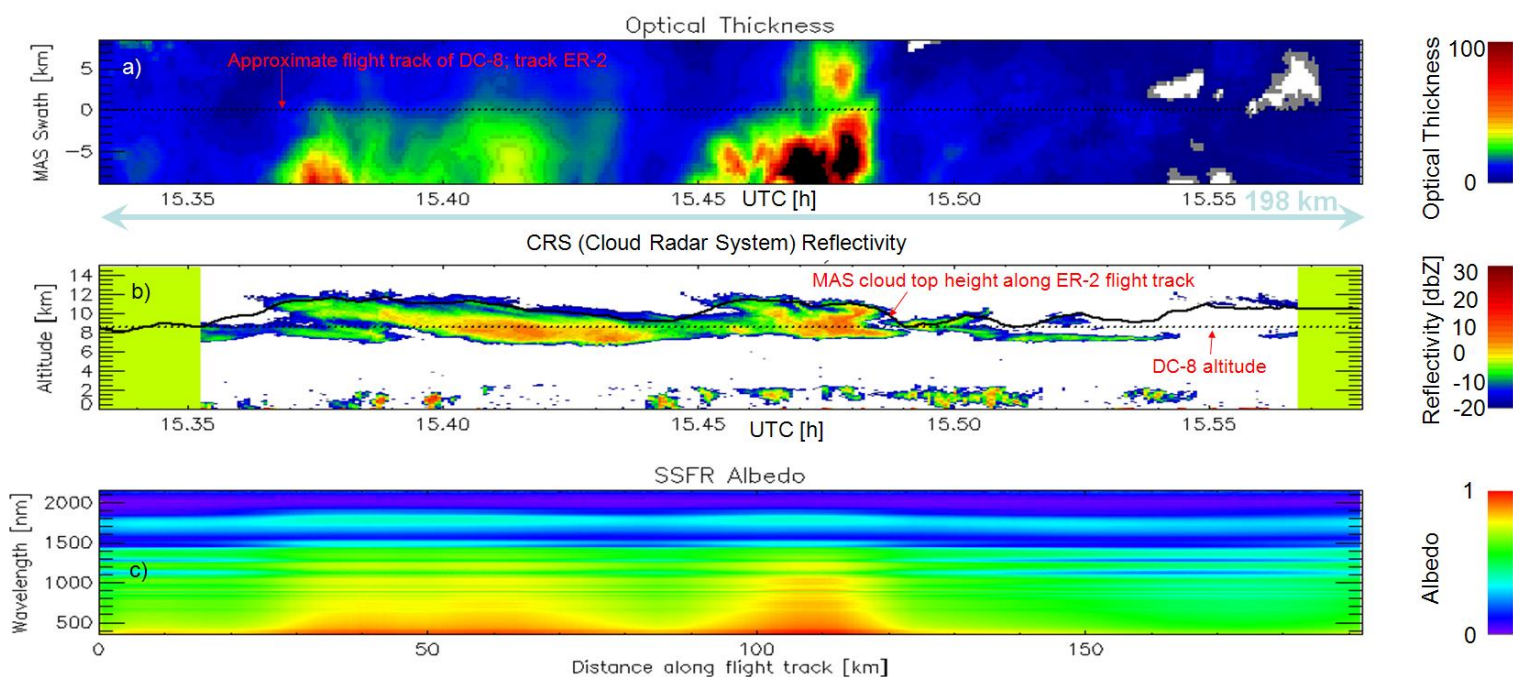
Figure 2 – Data along the 17 July flight track (1520 to 1535 UTC). Top panel (a): MAS-retrieved cloud optical thickness (total swath width 17.5 km) as viewed from above – the dotted line indicates the track of the DC-8 and ER-2 in the middle of the MAS swath; below (b): radar reflectivity from CRS in dBZ (side view). Regions with no data available are marked in light green. Cloud top height from MAS along the ER-2 flight track is over-plotted as thick black line; the dotted line indicates the approximate flight altitude of the DC-8. Bottom panel: ER-2 albedo (wavelength vertical dimension) along the flight track.

967
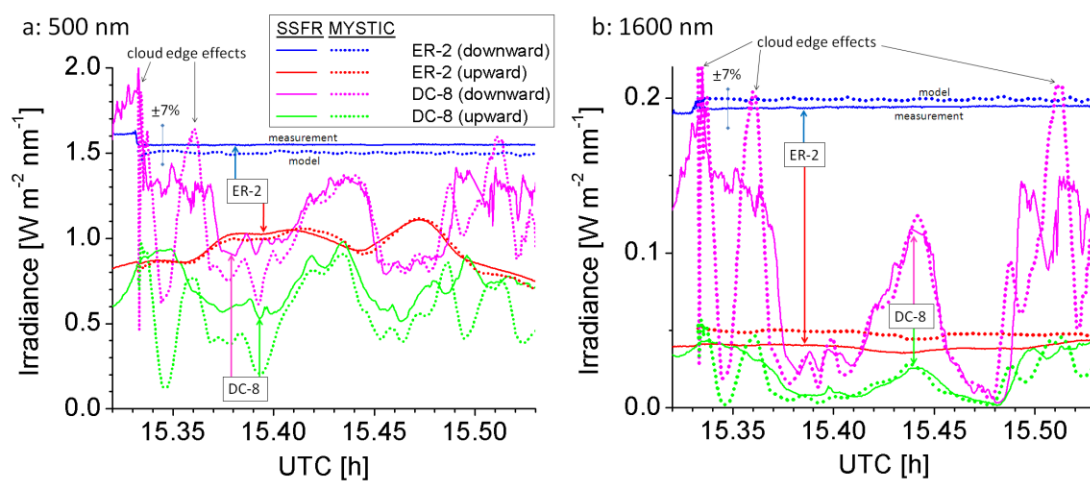
968 **Figure 3** – Time series of downward and upward irradiance (a: 500 nm, b: 1600 nm) measured onboard the

969 DC-8 and ER-2 (solid lines), along with the 3D model results (dotted lines).

970

971
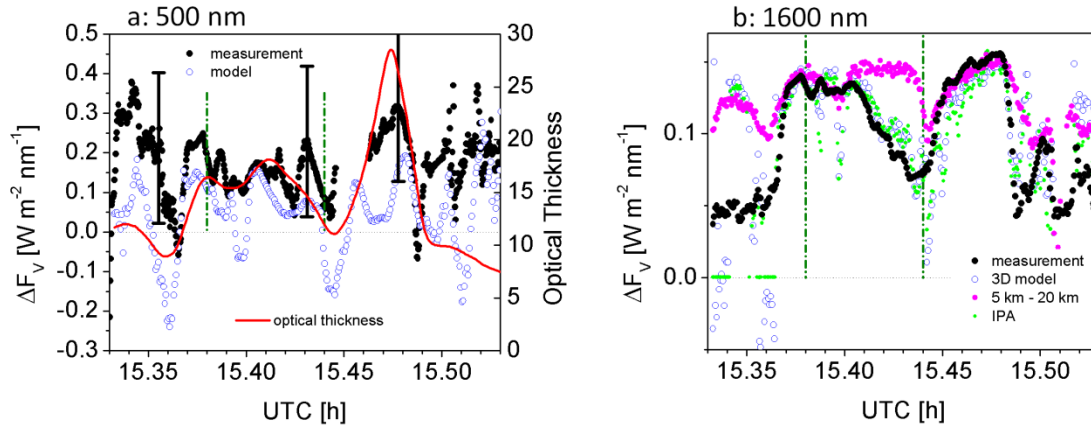
972

973 **Figure 4** – a: Time series of measured (black dots) and modeled (blue dots) vertical difference of net

974 irradiances at 500 nm, along with SSFR-footprint-averaged optical thickness (red line). The dash-dotted

975 green lines at UTC = 15.35 h and UTC = 15.44 h mark where spectra of ΔF_V are shown in Figure 7.

976 b: The same at 1600 nm. In addition, IPA results are shown (green symbols). The magenta symbols show

977 the model results for ΔF_V for the layer from 5 km to 20 km, rather than the standard 9 km (DC-8 altitude)

978 to 20 km (ER-2 altitude).
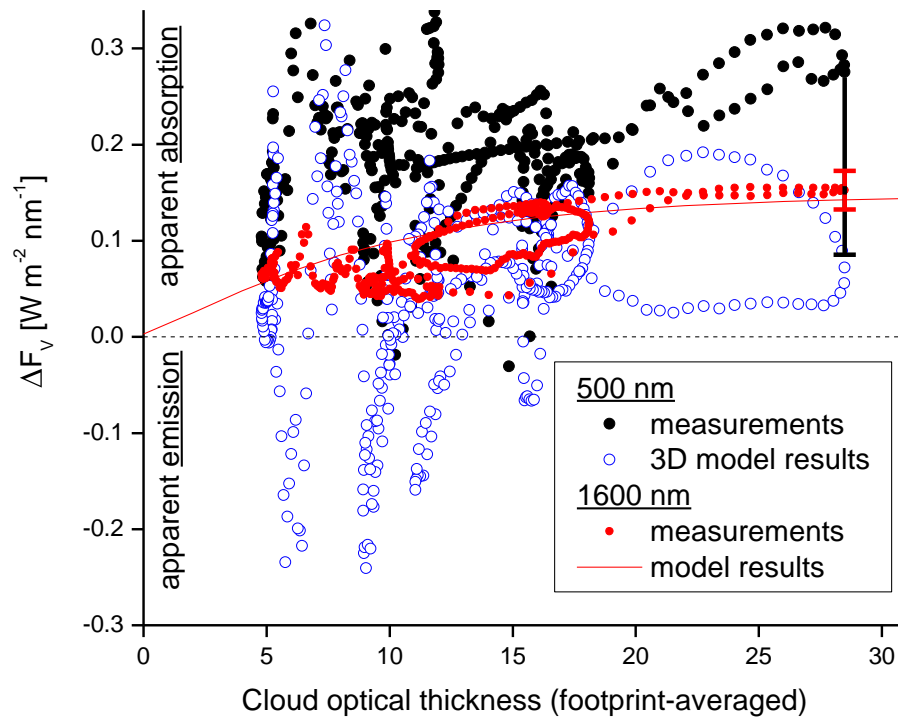
Figure 5 – Measured (black dots) and modeled (blue dots) vertical difference of net irradiances at 500 nm as a function of SSFR-footprint-averaged optical thickness. For comparison, the measurements at 1600 nm are shown (red dots) along with the model true absorption (red line).
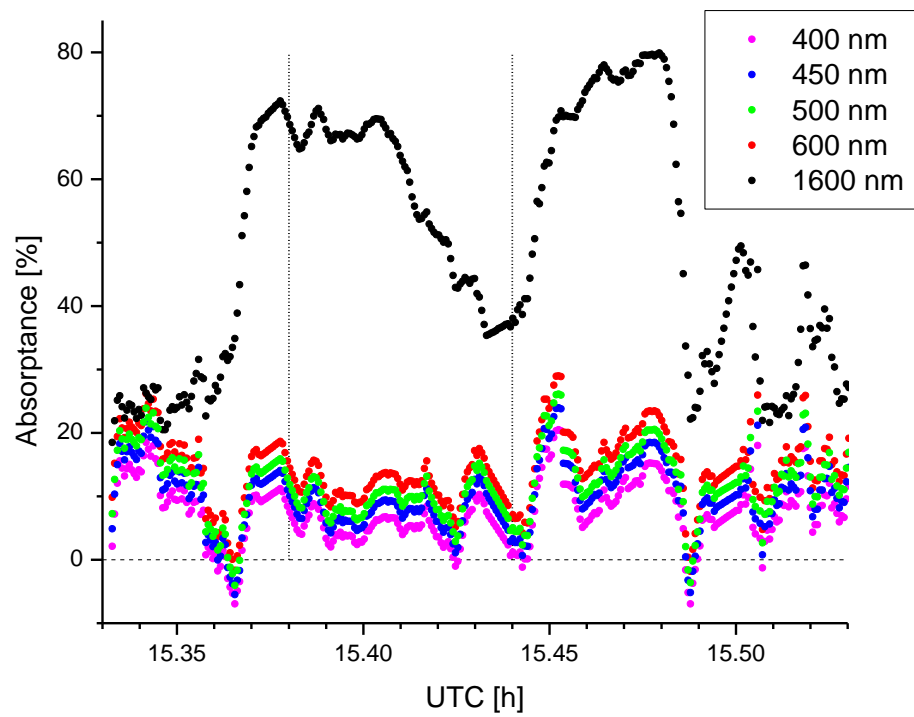
984
985   **Figure 6** – Measured apparent layer absorptance at wavelengths from 400 nm to 1600 nm.

986
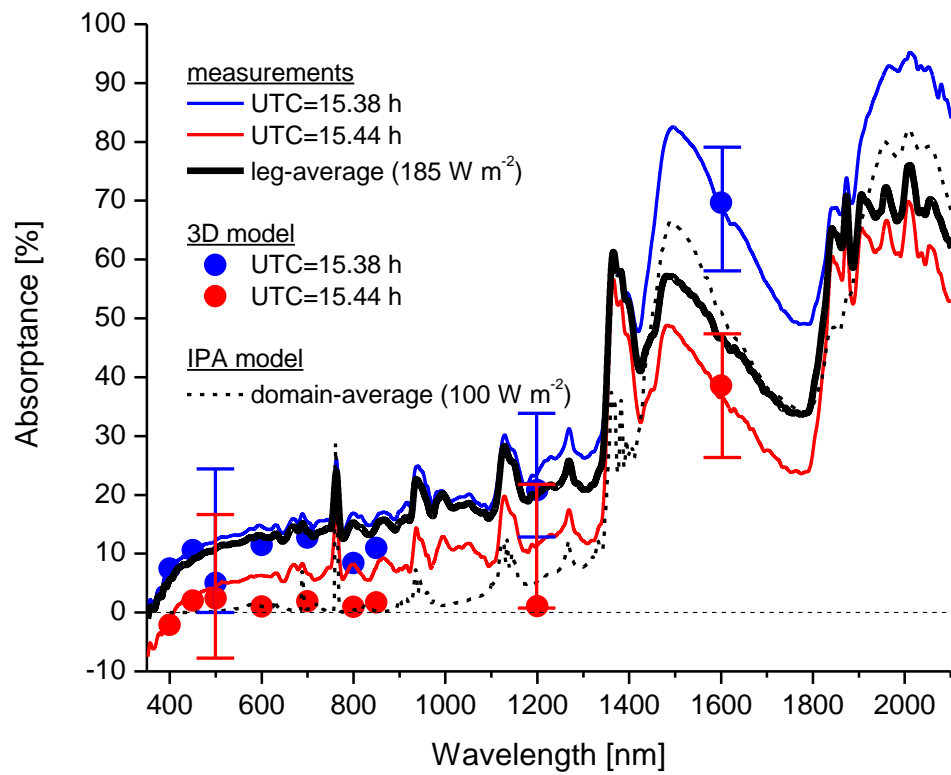
987 **Figure 7 –** Spectral absorptance (or fractional absorption) at two selected points along the flight track

988 (UTC = 15.44 h – optically thin region, and UTC = 15.38 h – optically thick region). The lines show the

989 measurements with ice absorption bands around, for example, 1500 nm. The symbols show 3D model

990 results.